


## Collisional ionization and recombination in degenerate plasmas beyond the free-electron-gas approximation

G. O. Williams\* and M. Fajardo

*GoLP/Instituto de Plasmas e Fusão Nuclear-Laboratório Associado, Instituto Superior Técnico, Universidade de Lisboa, 1049-001 Lisboa, Portugal*

 (Received 10 May 2020; revised 13 July 2020; accepted 15 November 2020; published 8 December 2020)

One of the most successful ways to model the multitude of electron and photon processes in plasmas is the approach used in collisional radiative (CR) codes. The accuracy of CR codes depends largely on the accuracy of the rates of each process. These rates are generally well approximated in hot, classical plasmas. However, in degenerate plasmas quantum effects can influence these rates and must be accounted for. Previous approaches have developed corrections to the classical rates using the free-electron-gas (FEG) approximation. Here, we use electronic structures beyond the FEG approximation and show how the collisional rates are affected by degeneracy in aluminum and iron plasmas. We find that the FEG is a good approximation for aluminum, whereas more complex electronic structures that include  $d$  orbitals, such as iron, deviate from the FEG approximation. This results in different degeneracy corrections to the collisional rates relative to those for the FEG. Although the general trend of the corrections to degenerate plasmas is captured by assuming an FEG, we show that more complex electronic structures can result in deviations, even outside the degenerate regime. This study further advances the treatment of free-electron quantum effects in collisional radiative models.

DOI: [10.1103/PhysRevE.102.063204](https://doi.org/10.1103/PhysRevE.102.063204)

### I. INTRODUCTION

The discovery that interacting fermions cannot occupy the same quantum state, degeneracy, has been a central tenet of modern physics. This law, the Pauli exclusion principle, forms the basis of our understanding of a wide range of physical systems, from the microscopic properties of modern electronics to the macroscopic behavior of neutron stars [1]. In plasmas, where high temperatures tend to pervade, the free electrons are not affected by this constraint, and classical approaches suffice. Yet there exists a range of plasmas in which quantum effects in the free-electron distribution cannot be ignored, referred to as degenerate plasmas. For example, these plasmas occur in solids heated to any temperature below a few times their Fermi energy, highly compressed matter found in brown dwarfs, and laser-driven nuclear implosions [2].

Most plasmas consist of atoms and ions with different charge states and electron configurations. In thermal equilibrium, the ratio of these charge states can be approximated by the Saha-Boltzmann relation [3]. However, this description does not capture the dynamics that dictate nonequilibrium and time-dependent effects that give rise to the plasma emission spectrum. This requires a method that accounts for the plethora of atomic processes in a time-dependent manner. To this end, rate equations coupled with detailed energy levels can be used to calculate all atomic processes in a so-called collisional radiative (CR) code. CR codes have been extremely successful at treating a wide range of plasmas, from

laser fusion to astrophysical objects [4]. Time-dependent CR codes use tabulated or measured electron energy levels, cross sections, and oscillator strengths from which the rates of transitions are calculated at a given temperature and density [5]. The tabulated data used in CR codes comes from experimental data where available, and calculated parameters from *ab initio* atomic codes such as FAC [6] and HULLAC [7]. A detailed emission spectrum can be calculated with CR codes using the rates of all the radiating processes. These codes are efficient and can be coupled to hydrodynamic codes to model the emission spectra from highly dynamic and nonequilibrium systems such as laser-driven fusion [8]. One drawback of CR codes is that microscopic plasma effects (how neighboring electrons and atoms affect the atomic processes) and their impact on the rates are not included directly. Previous studies have identified several mechanisms that can influence the collisional rates, including increased collisional ionization [9–12] and a reduction of three-body recombination rates due to the plasma medium (surrounding potential energy) [13,14]. Other studies have shown that certain microscopic effects can be included in a parameterized manner in CR codes for ionization potential depression [15,16] and spectral line broadening [17].

Recently, it was shown that the rates of collisional processes are reduced by an order of magnitude in degenerate plasmas [4,18–20]. This reduction is attributed to one of the fundamental laws of quantum mechanics, the Pauli exclusion principle [1]. This law shapes the degenerate free-electron distribution and can act to block certain electron transitions to already filled states (Pauli blocking). The quantum statistics of free electrons, as introduced by Fermi and Dirac in 1926 [21,22], led to the development of the *free-electron-gas* (FEG) model [23]. The FEG model can predict the degenerate

\*garth.williams@tecnico.ulisboa.p

electron energy distribution and Pauli blocking at a given electron density and temperature. Despite its usefulness, its applicability is limited due to the assumption of independent electrons that do not interact with the ions or other electrons. Therefore any electronic structure due to ion potentials, crystal structure, or electron-electron interactions is lost. For example, this may be a reasonable approximation of the  $s$  and  $p$  conduction bands in metals. However, this assumption is not valid for electronic structures that include  $d$ -orbital electrons. A robust and tractable approach to correcting classical rates for degeneracy effects has been previously demonstrated [4,18,19,24]. Yet to date, these corrections have used the FEG approximation for free electrons [4,18,19]. This is a good approximation for simple metals with  $s$  and  $p$  free-electron orbitals such as aluminum, however, the electronic structure varies significantly from an FEG for transition-metal elements such as iron, which include strongly localized  $d$  orbitals. Calculating the electronic structure of an arbitrary arrangement of elements in space has been made possible with density functional theory (DFT). Although DFT can include degeneracy, bound electrons, and free electrons, modeling the plasma dynamics that give rise to an emission spectrum is currently not possible with DFT. This is largely because DFT does not include the exact electron-electron interaction that gives rise to collisional ionization or recombination, or the radiative processes responsible for the plasma emission spectrum. All electron-electron interactions not treated in the DFT framework must be approximated in the so-called exchange-correlation (XC) functional. The time-dependent DFT can include external electromagnetic fields, but standard treatments are adiabatic and cannot treat energy exchange between the field and the plasma. A time-dependent DFT approach that includes highly accurate nonadiabatic XC functionals and an external field could, in principle, give accurate time-dependent information on the electron motion in time and space. However, radiation from plasma self-emission would still not be modeled explicitly and would have to be inferred by tracking the electrons in space and time. Furthermore, the computational cost of running such a calculation is not currently practical.

It has been shown that the inclusion of FEG statistics can change significantly the rates of collisional processes. However, the question of how more complex electronic structures, such as iron, affect the rates in degenerate plasmas has not yet been addressed.

Here, we determine the degeneracy correction factors for collisional ionization and three-body recombination and investigate the sensitivity of the correction factors to the free-electron energy distribution and ionization cross section. Two elements are chosen for their contrasting electronic structures: aluminum, as it displays an electronic structure that is well approximated by an FEG with minor deviations; and iron, as its electronic structure deviates strongly from that of an FEG. The density of states (DOS) defines the number of available states in a given range of electron energies. We calculate the DOS of aluminum and iron using ground-state DFT calculations. These electronic structures are used in place of the FEG DOS to calculate the correction factors of the collisional rates of ionization and three-body-recombination following previous formulations [4,18–20,24].

We find that although the normally applied FEG correction factors are a good first approximation for simple electronic structures, differences occur for more complex elements, especially under conditions close to the transition between the degenerate and the classical regimes. As the correct cross section under degenerate conditions and its dependence on temperature and density are largely unknown, we investigate the sensitivity of the degeneracy corrections on the form of the cross section. In particular, we show that the weighting of the cross section on the electron energy increases the magnitude of the correction factor. The article is outlined as follows: in Sec. II, we map out the degenerate regime and detail the methods used to calculate the correction factors; in Sec. III, we describe the DFT calculations used to obtain the DOS of aluminum and iron; in Sec. IV, we use the DOS from the DFT calculations to calculate the correction factors for aluminum and iron and compare them with those calculated using the FEG DOS; and in Sec. V we conclude.

## II. COLLISIONAL RATES AND DEGENERACY

In this section we detail the calculation of the correction factor. All atomic processes involving the free-electron distribution will be affected by degeneracy, however, here we focus on the two processes which dominate the charge-state distribution in dense plasmas where degeneracy is most relevant, that is, collisional ionization and the inverse process, three-body recombination. The rates of these processes are determined by the distribution of the free electrons,  $f(E)$ , and the cross section of the process in question,  $\sigma(E)$ . Following closely the formalism of Tallents [18], we express the difference in rates as the ratio of the degenerate and classical rates.

The first effect of degeneracy we consider is the shape of the electron energy distribution function. The distribution of classical particles in energy,  $E$ , in thermal equilibrium is described by Maxwell-Boltzmann (MB) statistics. In SI units of number density per unit energy ( $\text{m}^{-3} \text{J}^{-1}$ ) the MB electron energy distribution function is given as

$$f(E)^{\text{MB}} = \frac{2n_e}{\sqrt{\pi}} \frac{1}{(k_B T_e)^{3/2}} \sqrt{E} \left[ \frac{1}{\exp\left(\frac{E}{k_B T_e}\right)} \right]. \quad (1)$$

Fermi-Dirac statistics give the occupation probability of a state including the degeneracy of available states for particles of half-integer spin, such as electrons [term in square brackets in Eq. (2)]. The DOS of an FEG is given by the term outside the square brackets in Eq. (2). The distribution of energy of particles in an FEG is the DOS multiplied by the Fermi-Dirac probability distribution and is given by

$$f(E)^{\text{FEG}} = 4\pi \left( \frac{2m_e}{h^2} \right)^{3/2} \sqrt{E} \left[ \frac{1}{1 + \exp\left(\frac{E-\mu}{k_B T_e}\right)} \right], \quad (2)$$

where  $n_e$  is the electron number density,  $m_e$  is the electron mass,  $h$  is Planck's constant,  $k_B$  is Boltzmann's constant,  $\mu$  is the chemical potential, and  $T_e$  is the electron temperature.

The chemical potential,  $\mu$ , in Eq. (2) must be such that the electron density is conserved. To determine the correct  $\mu$  for a given temperature and density, we iterate values of  $\mu$  until

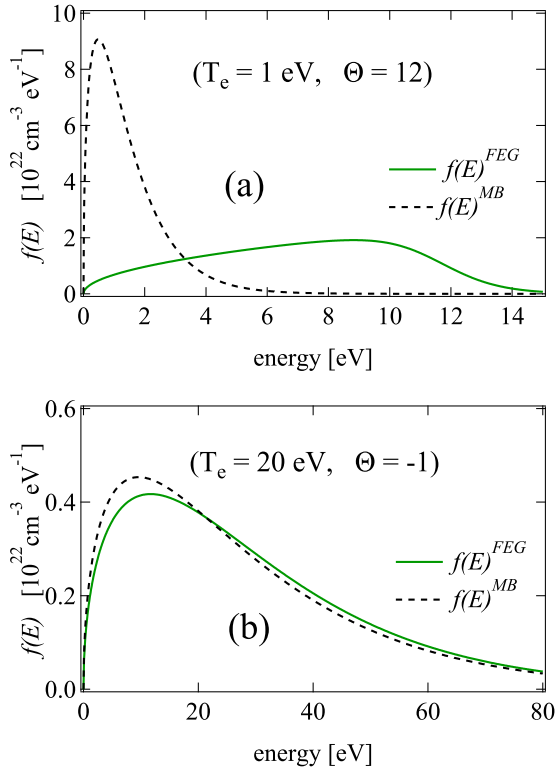


FIG. 1. (a) Comparison of electron energy distributions in the strongly degenerate regime ( $\Theta = 12$ ) for FEG [solid green line; Eq. (2)] and MB [dashed black line; Eq. (1)] statistics. (b) Comparison of electron energy distributions in the classical regime ( $\Theta = -1$ ) for FEG [solid green line; Eq. (2)] and MB [dashed black line; Eq. (1)] statistics. The electron density used was  $n_e = 1.8 \times 10^{23} \text{ cm}^{-3}$ , to match that of solid aluminum.

we reach the required density, satisfying the relation

$$\int f(E)^{\text{FEG}} dE = n_e. \quad (3)$$

To quantify the level of degeneracy, we use the parameter

$$\Theta = \frac{\mu}{k_B T_e}, \quad (4)$$

where increasingly positive values of  $\Theta$  correspond to increasing degeneracy, and increasingly negative values of  $\Theta$  correspond to increasingly classical plasmas.

Figure 1 shows a comparison of the electron distributions for Eqs. (1) and (2) at two temperatures representative of the degenerate and classical conditions. In the degenerate regime ( $T_e = 1 \text{ eV}$ ) shown in Fig. 1(a) a striking difference between the two electron energy distribution functions is evident. The FEG distribution restricts the occupation at lower energy levels due to degeneracy, whereas the MB distribution does not restrict electron occupation at lower electron energy levels. At higher temperatures ( $T_e = 20 \text{ eV}$ ) the difference between the FEG and the MB distributions is negligible [Fig. 1(b)]. This shows that considerable differences between  $f(E)^{\text{MB}}$  and  $f(E)^{\text{FEG}}$  can occur at lower temperatures.

In Fig. 2 we show the level of degeneracy,  $\Theta$ , using the FEG approximation and plot it as a function of the electron temperature and density, which are accessible through

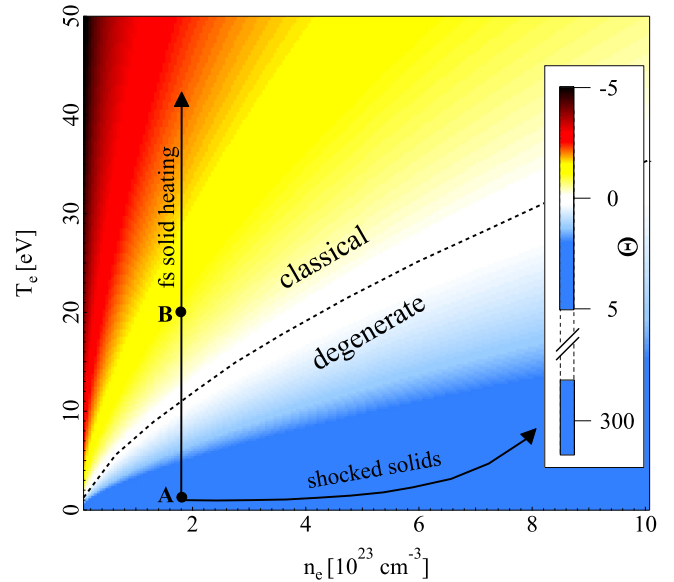


FIG. 2. The degeneracy parameter,  $\Theta$ , for a range of electron temperatures,  $T_e$ , and electron densities,  $n_e$ , for an FEG. Possible conditions of a short pulse laser and XFEL heated solids and shocked solids are shown with arrows. The dashed line separates the classical and degenerate regimes. The electron distribution corresponding to point A and point B is shown in Figs. 1(a) and 1(b), respectively.

laser experiments. The dashed curve corresponds to  $\Theta = 0$ , separating the degenerate and classical plasmas, respectively. Points A and B correspond to electron distributions under the same conditions as in Figs. 1(a) and 1(b), respectively.

Femtosecond XFEL heating has become a novel method of isochorically heating solids to plasma conditions [25,26] or highly nonequilibrium states [20,27]. Ramp compression has recently been shown to increase the density to several times that of a solid at room temperature [28], creating previously unexplored phases of degenerate matter in the laboratory. In Fig. 2, it is clear that short-pulse laser heating and compression experiments both traverse the degenerate regime to some degree.

Figure 3 compares how degeneracy varies with the temperature and density of iron (the calculation of the DOS of Fe is presented in Sec. III). In Fig. 3, there is a more abrupt transition to the classical regime as the temperature increases, due to differences in the DOS of iron compared to the FEG.

Figures 2 and 3 suggest that, under typical accessible laboratory conditions, degeneracy effects are important at temperatures below  $\sim 20 \text{ eV}$ . Iron and aluminum in their solid state have their first ionization energies at around 72 and 52 eV, respectively. The temperatures required to reach the first ionisation state above their solid state values is approximately  $T_e = 15 \text{ eV}$  for iron and  $T_e = 25 \text{ eV}$  for aluminum. This could suggest that significant levels of ionization generally only occur for temperatures that are in the classical regime. However, the path of converting a solid into a plasma state always traverses the degenerate regime. For example, nonequilibrium heating induced by optical lasers or XFELs typically creates a nonthermal electron distribution with hot-electron energies well above the collisional

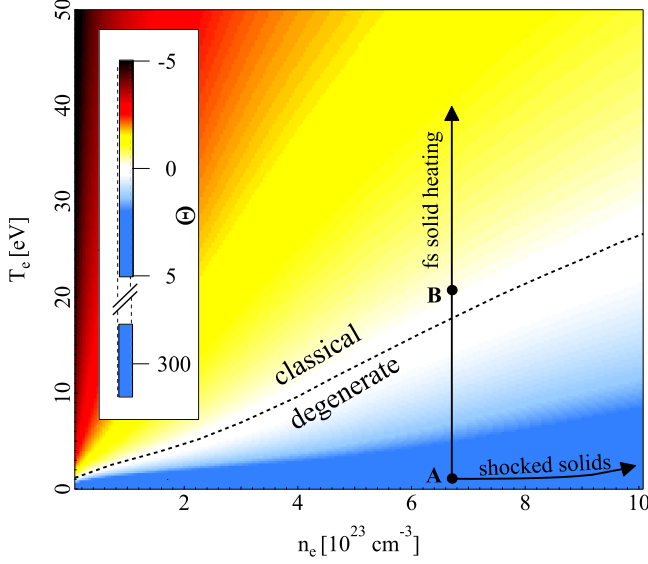


FIG. 3. The degeneracy parameter,  $\Theta$ , for a range of electron temperatures,  $T_e$ , and electron densities,  $n_e$ . Possible conditions of a short pulse laser and XFEL heated solids and shocked solids are shown with arrows. The electron distribution corresponding to point A and point B is shown in Figs. 8(a) and 8(b), respectively.

ionization threshold. In such scenarios, the early stages of heating are characterized by hot electrons relaxing in a strongly degenerate plasma, making degeneracy effects important in nonthermal scenarios. Furthermore, the shape of the electron distribution can retain quantum features (such as localized  $d$  orbitals) even under conditions considered classical,  $\Theta < 0$  (discussed further here and in Sec. III).

To investigate how degeneracy affects collisional processes, we consider collisional ionization by an incoming electron of energy  $E$ , of a bound electron that requires an energy  $E_i$ , to be ejected. The incoming electron,  $E$ , is scattered to energy  $E'$  and the ionized electron is scattered to energy  $E''$ , yielding the energy balance

$$E = E' + E'' + E_i. \quad (5)$$

The classical collisional ionization rate per second for a total ionization cross section  $\sigma(E)^{\text{CI}}$ , ionization energy  $E_i$ , electron distribution  $f(E)^{\text{MB}}$ , and velocity  $v(E)$  is given as

$$R_C^{\text{CI}} = \int \sigma^{\text{CI}}(E)v(E)f(E)^{\text{MB}}dE. \quad (6)$$

The classical rate of recombination per second for a three-body recombination cross section is generally given as

$$R_C^{\text{3BR}} = \iiint v(E')v(E'')f(E')^{\text{MB}}f(E'')^{\text{MB}}\sigma \times (E, E')^{\text{3BR}}dEdE'dE'', \quad (7)$$

where the differential three-body recombination cross section,  $\sigma(E, E')^{\text{3BR}}$ , depends on the energies  $E$  and  $E'$  and is in units of  $\text{m}^4 \text{s}$ .

To calculate the collisional rate for a degenerate plasma, we include the two principal quantum effects by using a

degenerate electron distribution and the effect of Pauli blocking. The degenerate electron distribution is included by inserting a degenerate form of  $f(E)$  and using the appropriate chemical potential,  $\mu$ . Aside from the FEG distribution having a different shape than the MB distribution, another phenomenon, Pauli blocking, must also be included in the collisional rate equations. Pauli blocking has its origin in the same quantum effect that determines the shape of the distribution, the Pauli exclusion principle. This can block electrons transitioning to already occupied states. To a first approximation, the effect of Pauli blocking can be calculated once the Fermi-Dirac distribution is known. The probability,  $P(E)$ , of a vacant final state at energy  $E$  can be written as

$$P(E) = 1 - \frac{1}{1 + \exp\left(\frac{E-\mu}{k_B T_e}\right)}, \quad (8)$$

so that when a state at  $E$  is completely vacant,  $P(E) \approx 1$ , and when a state at  $E$  is fully occupied,  $P(E) \approx 0$ . Equation (8) is used to calculate the blocking factors for both the FEG and the DFT rate calculations. This assumes that the probability of electron transition is proportional to the degree of occupation alone. A more accurate approach would be to include the matrix elements for every possible transition into the blocking factor, however, this is likely to be a small refinement compared to the overall degeneracy correction factor and its dependence on  $f(E)$  or the cross section.

To include degeneracy effects in the collisional ionization process, we must include a degenerate electron distribution function and Pauli blocking for the two outgoing electrons,  $E'$  and  $E''$ . We include a degenerate distribution by inserting Eq. (2) into Eq. (6) and include the blocking factors from Eq. (8) for all possible outgoing electron configurations in Eq. (6). For collisional ionization, the degenerate collisional rate is

$$R_Q^{\text{CI}} = \int_{E_i}^{\infty} v(E)f(E)^{\text{FEG}}\sigma(E)^{\text{CI}} \times \left[ \frac{\int_0^{E-E_i} P(E')P(E'')dE'}{\int_0^{E-E_i} dE'} \right] dE. \quad (9)$$

In Eq. (9), the limits of integration over  $E$  begin at the minimum possible ionization energy  $E_i$  and continue to any available energy above this threshold. Since  $E'' = E - E' - E_i$ , for any given incoming energy  $E$ , there exists a definite combination of outgoing electron energies  $E'$  and  $E''$  that obey this relation, defining the integration to a one-dimensional range of  $E'$  and  $E''$  pairs. The integration spans all possible values of  $E'$ , from 0 to the maximum energy of  $E'$ , which is  $E - E_i$  (this occurs when  $E'' = 0$ ). The introduction of a further integral over the ejected energy  $E'$  in Eq. (9) requires the inclusion of a normalization factor in the denominator,  $\int_0^{E-E_i} dE'$ , when using the total cross section,  $\sigma(E)^{\text{CI}}$ . If the differential cross section is used, this normalization is not required and the differential cross section,  $\sigma(E, E')^{\text{CI}}$ , can be inserted into the integral over  $E'$  in Eq. (9).

By similar arguments, the three-body recombination rate for a degenerate plasma is given as

$$R_Q^{3BR} = \int_{E_i}^{\infty} \left( \frac{\int_0^{E-E_i} \sigma(E)^{3BR} v(E') v(E'') f(E')^{FEG} f(E'')^{FEG} dE'}{\int_0^{E-E_i} dE'} \right) P(E) dE. \quad (10)$$

The recombining electron lies somewhere in the distribution  $f(E')$  and transitions to a vacant level at energy  $E_i$ . The energy liberated from this  $E' \rightarrow E_i$  transition is given up to another electron,  $E''$ , in the free-electron distribution that makes the transition  $E'' \rightarrow E$ , and this electron is subject to Pauli blocking.

We can now express the difference of the collisional processes of Fermi-Dirac and Maxwell-Boltzmann statistics as a simple ratio given by

$$CF^{CI} = \frac{R_Q^{CI}}{R_C^{CI}} \quad \text{and} \quad CF^{3BR} = \frac{R_Q^{3BR}}{R_C^{3BR}}. \quad (11)$$

The rate of collisional ionization is related to its inverse process, three-body recombination, through the law of detailed balance for degenerate plasmas,

$$\frac{R_Q^{3BR}}{R_Q^{CI}} = \frac{g_i}{g_f} \exp\left(\frac{\mu + E_i}{k_B T_e}\right), \quad (12)$$

where  $g_i$  and  $g_f$  are the statistical weights of the initial and final states, respectively.

We now consider various forms of the collisional ionization cross section,  $\sigma(E)$ . Some of the most widely used collisional ionization cross sections are an empirical fit to data from low-density plasma experiments. These cross sections are usually given in terms of the total cross section,  $\sigma(E)^{CI}$ , which is only dependent on the incoming electron energy,  $E$  [29]. The form of the total cross section given by Lotz [29,30] is considered a good approximation for classical plasmas.

We note that the error in the magnitude of the cross section does not impact this study because this error is canceled in the ratio. However, the overall shape of the cross section is important, as the rate is sensitive to where in the electron distribution,  $f(E)$ , the cross section is weighted. Thus, we perform this study for two plausible cross-section shapes, an analytic cross section and a Lotz cross section, to see how the shape affects the correction factor. This sensitivity study is essential because we currently do not know exactly how the cross-section shapes are altered under extreme conditions. The cross sections used here do not incorporate any dependence on temperature or density. A more complete model of the cross section would take into account the colliding electron wave functions and their dependence on the plasma environment. The influence of plasma density effects on the collisional ionization cross section has been investigated elsewhere, and it has been shown that the plasma potential can modify the shape of the collisional ionization cross section [11,31]. The inclusion of a cross section that is fully self-consistent with the plasma environment is outside the scope of this study. However, to illustrate the role of the cross-section shape in the degeneracy correction factor, we

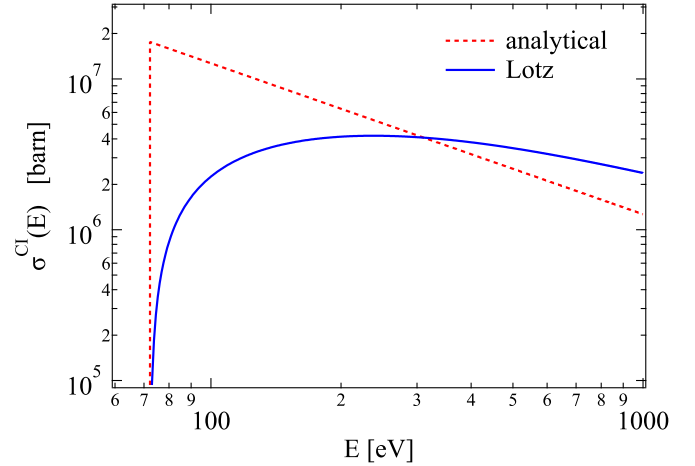


FIG. 4. The collisional ionization cross section,  $\sigma^{CI}(E)$ , as a function of the incoming electron energy,  $E$ , for the Lotz cross section [from Eq. (14)] and analytical cross section [from Eq. (13)].

use two significantly contrasting cross-section shapes in the calculation of the rates.

We have tested cross sections that have a dependence on the outgoing electron energies for a limited range of conditions and found that the shape and resulting rates are very similar to those when the cross section of Lotz is used. However, we have found large differences when deviations from the shape of the Lotz cross section are more striking. To highlight the role of the shape of the cross section, we use two cross sections that have markedly different shapes: a relatively simple cross section, which we term the analytical cross section, given by

$$\sigma(E)^{ana} = A \frac{4\pi a_0^2 E_{ion}}{E}, \quad (13)$$

and the cross section of Lotz [29,30], given by

$$\sigma(E)^{Lotz} = a_i \frac{\ln(E/E_i)}{E E_i} \{1 - b_i \exp[-c_i(E/E_i - 1)]\}. \quad (14)$$

In Eq. (13),  $A = 0.05$  is an arbitrary scaling constant used to make the cross section on the same scale as the Lotz. In Eq. (14),  $a_i$ ,  $b_i$ , and  $c_i$  are empirical scaling constants and dependent on the species and ionization level. We use  $a_i = 4\pi a_0 R_y^2$ , where  $a_0$  is the Bohr radius and  $R_y$  the Rydberg energy. The variable  $q_i$  is the number of electrons in the ionized shell. We take the case of aluminum as an example and use the values of  $a_i$ ,  $b_i$ , and  $c_i$  from [29] to show the form of the cross section in Fig. 4. Interestingly, fluorescence experiments in the degenerate regime have suggested that correction factors using the analytical cross section in Eq. (13) give a better fit to the data [20], whereas the cross section of Lotz in Eq. (14) is more representative of the generally accepted cross-section shape, albeit in the classical regime. As the exact form of the cross section under degenerate conditions remains largely unknown, we include both the analytical and the Lotz cross sections to compare the impact of their contrasting shapes on the correction factors.

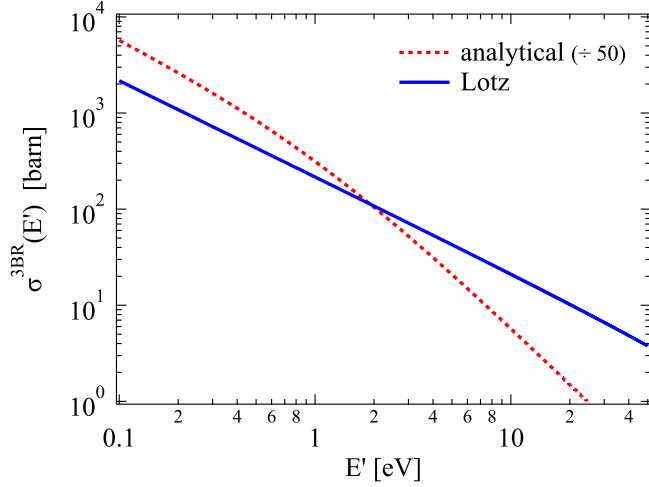


FIG. 5. The three-body recombination cross section,  $\sigma^{3\text{BR}}(E')$ , as a function of the recombining electron energy,  $E'$ , for the Lotz and analytical cross sections. The three-body recombination cross sections are calculated from the collisional ionization cross sections given by Eqs. (13) and (14) and using the relation in Eq. (15). An electron energy of  $E'' = 1$  eV and electron density of  $n_e'' = 10^{23}$  cm $^{-3}$  was used to calculate  $\sigma^{3\text{BR}}(E')$ . The slope of the analytical cross section is steeper than that of the Lotz cross section and favors recombination with lower-energy electrons, giving greater differences in the three-body recombination rates for the MB and FEG distributions. For purposes of comparison the analytical cross section has been divided by 50.

Experiments or calculations of the three-body recombination cross section are greatly lacking in the literature. However, we can relate the collisional ionization cross section to the three-body recombination cross section through the Fowler relation [32],

$$\sigma(E, E')^{3\text{BR}} = \frac{g_i}{g_f} \frac{16\pi m_e}{h^3} \frac{E}{E'E''} \sigma(E', E)^{\text{CI}}. \quad (15)$$

From Eq. (15), it is clear that the differential cross section,  $\sigma(E', E)^{\text{CI}}$ , is required to calculate  $\sigma(E, E')^{3\text{BR}}$ . We assume no dependence of the cross section on the outgoing electron energies. The total cross section is calculated from the differential cross section by

$$\int \sigma(E, E') dE' = \sigma(E). \quad (16)$$

In Fig. 5 we show the three-body recombination cross section as a function of the recombining electron  $E'$  for a given flux of electrons ( $E'' = 1$  eV and  $n_e'' = 10^{23}$  cm $^{-3}$ ). We note that the difference between the Lotz and the analytical cross sections in Fig. 5 is the preferential weighting of lower electron energies for the analytical cross section. Collisional ionisation is driven by electrons above  $E_i$  in  $f(E)$ , whereas three-body recombination is most sensitive to the lowest-lying electrons in the  $f(E)$ .

In this section we have shown how the degenerate rates are calculated for FEG and MB distributions. In Sec. III we

outline the calculation of the DOS for real elements outside the FEG approximation.

### III. DENSITY FUNCTIONAL THEORY CALCULATION OF THE FREE-ELECTRON ENERGY DISTRIBUTION FUNCTION

In this section we present calculations of the DOS of aluminum and iron using density functional theory. In DFT, a numerical scheme is used to converge to the electron density that minimizes the total energy. This electron density is then represented by a set of independent one-electron (Kohn-Sham) wave functions. These wave functions have a characteristic energy and crystal momentum. The density of states is calculated by summing all the available momentum states (in the first Brillouin zone) within a given energy range. The number of available states can then be represented as a function of the energy. Once the DOS is obtained from the DFT calculation, it can be populated using Fermi-Dirac statistics at a given temperature and density [Eq. (2)]. The chemical potential is generally unknown for arbitrary temperatures and densities and, therefore, must be found iteratively using Eq. (3) (conservation of mass) as a constraint.

The applicability of DFT to higher electron temperatures was first shown by Mermin [33]. In principle, the electronic structure of the noninteracting electron system can be exact using the Mermin-Kohn-Sham equations if the appropriate temperature-dependent XC functional is known. The standard ground-state approximation of the XC functional has been shown to be a reasonable starting point for warm dense matter studies [34], yet clear deficiencies have also been demonstrated [35]. For a more detailed discussion on finite-temperature DFT see [36]. Here, we use the standard ground-state approximation to the XC functional in the Mermin framework of finite-temperature DFT.

Although an exact band-structure match for any given material cannot be expected from a standard DFT calculation, the overall shape of the free-electron DOS is captured with sufficient accuracy for this study. At solid densities and low temperatures, the DOS is not expected to differ significantly from that of a solid, whereas at higher temperatures the shape of the DOS will change due to ionization and electron delocalization. A rigorous treatment would require the DOS to be calculated at every combination of temperature and density. However, we have tested the DOS at temperatures of around  $T_e \approx 20$  eV for solid aluminum and iron, and the overall shape remains the same as that of a cold solid. The plasma density also shapes the DOS. We have calculated the DOS at densities of up to twice that of a solid, and apart from the expected smearing to higher energy levels, the overall shape remains the same.

We use the Vienna *Ab initio* Simulation Package (VASP) to perform the DFT and corresponding DOS calculations for aluminum and iron at solid densities of 2.7 and 7.7 g cm $^{-3}$ , respectively [37–41]. VASP uses a plane-wave basis set with pseudopotentials to calculate the Kohn-Sham orbitals. The calculations were carried out with the pseudopotentials supplied with VASP, using the projector augmented wave (PAW) method [41,42]. The generalized gradient approximation (GGA) of Perdew, Burke, and Ernzerhof was used as the

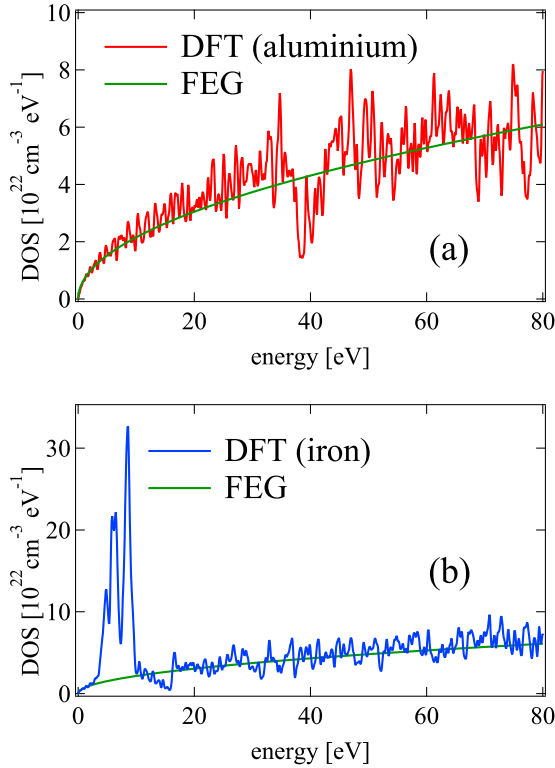


FIG. 6. The DOS of cold solid aluminum calculated using DFT (noisy solid red line) compared to that of an FEG (solid green line) (a). The DOS of cold solid-density iron calculated using DFT (noisy solid blue line) compared to that of an FEG (solid green line) (b). The electron density of aluminum is taken as  $1.8 \times 10^{23} \text{ cm}^{-3}$ , and the electron density of iron is taken as  $6.7 \times 10^{23} \text{ cm}^{-3}$ .

approximation to the XC energy for aluminum [43]. The GGA approximation of Ceperley and Adler was used for iron [44]. An  $8 \times 8 \times 8$   $k$ -point mesh was generated using the method of Monkhorst and Pack [45]. Four atoms were arrayed in a face-centered cubic unit cell for aluminum and a body-centered cubic for iron. We ignore spin polarization in the calculation of the electronic structure, as temperatures of interest for plasmas far exceed the Curie temperature at which ferromagnetic effects are negligible. Two subshells of bound electrons have been used in the calculation of the DOS. For iron this corresponds to the  $3s$  and  $3p$  levels, and for aluminum this corresponds to the  $2s$  and  $2p$  subshells. Although these bound electrons are included in the electronic structure calculation, we only use the free-electron structure for  $f(E)$  in our rate calculations.

In Figs. 6(a) and 6(b) we present the DOS calculations for aluminum and iron, respectively. The DOS of aluminum and iron are compared to the DOS of the FEG in both cases. The DOS is calculated as an integration over the allowed energy values that are sampled within the  $k$ -point grid. A smoothing of 0.1 eV is applied to the integration. The noisy appearance of the DOS is due to the finite  $k$ -point sampling. Further increasing the  $k$ -point grid increases the DOS accuracy and smooths the curve. For aluminum, the DOS is well approximated by the FEG up to about 40 eV, where a partial bandgap appears [Fig. 6(a)]. The Fermi energy for solid-density aluminum is

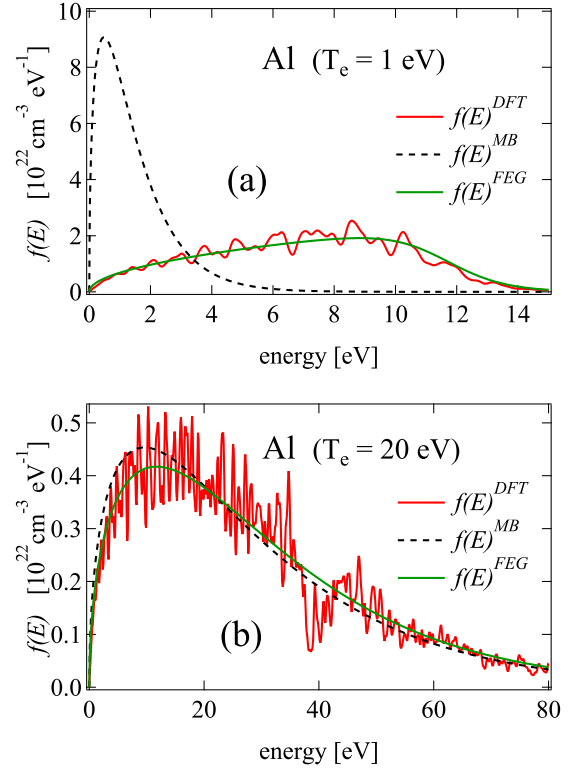


FIG. 7. The  $f(E)$  of cold solid-density aluminum for an FEG (solid green curve), calculated by DFT (noisy solid red curve) and according to MB statistics (dashed black line). The  $f(E)$  is shown (a) in the strongly degenerate regime ( $\Theta = 12$ ,  $T_e = 1 \text{ eV}$ ) and (b) in the classical regime ( $\Theta = -1$ ,  $T_e = 20 \text{ eV}$ ).

about 11.2 eV; as such, the partial bandgap of aluminum at 40 eV will only be significantly occupied at higher temperatures ( $T_e > 30 \text{ eV}$ ). For iron, the  $d$  orbitals result in peaks in the DOS that significantly surpass the number of states available in the FEG model [Fig. 6(b)]. The Fermi energy of iron is taken as 8.4 eV. The free-electron densities used for aluminum and iron were  $1.8$  and  $6.7 \times 10^{23} \text{ cm}^{-3}$ , respectively. At low electron energies, between 0 and 3 eV, and energies higher than  $\sim 20 \text{ eV}$ , the iron DOS is well approximated by the FEG. However, between 3 and 10 eV the strongly localized  $d$  orbitals contribute to a much higher DOS than the FEG.

The DOS determines the availability of electron states; these states are occupied according to Fermi-Dirac statistics, which is a function of the temperature and density. To compare the resulting treatments of the  $f(E)$ , we present the  $f(E)$  for the MB, FEG, and DFT approaches for aluminum in Fig. 7 and for iron in Fig. 8 for two contrasting temperature regimes,  $T_e = 1 \text{ eV}$  and  $T_e = 20 \text{ eV}$ . For aluminum at  $T_e = 1 \text{ eV}$  [Fig. 7(a)], the difference between the FEG and the MB is stark, as shown in Fig. 1. This is one of the two principal reasons to which we attribute the difference in the rates of collisional processes in the classical and degenerate regimes, the other being Pauli blocking. The  $f(E)^{\text{DFT}}$  varies insignificantly from the  $f(E)^{\text{FEG}}$  under these conditions. At  $T_e = 20 \text{ eV}$  [Fig. 7(b)] the three treatments of the FEG agree very well, aside from a small deviation around 40 eV for

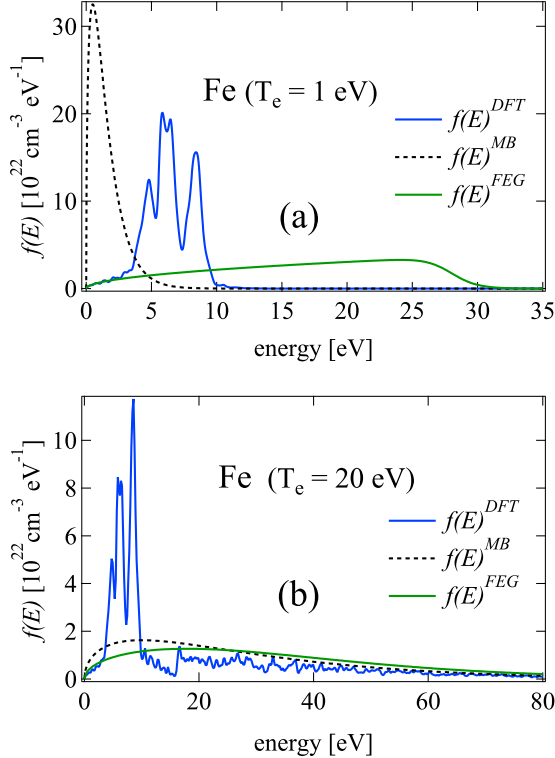


FIG. 8. The  $f(E)$  of cold, solid-density iron for an FEG (solid green curve), calculated by DFT (noisy solid blue curve) and according to MB statistics (dashed black line). The  $f(E)$  is shown (a) in the strongly degenerate regime ( $T_e = 1$  eV) and (b) at a temperature generally considered to be in the classical regime ( $T_e = 20$  eV) (b). An electron density of  $6.7 \times 10^{23} \text{ cm}^{-3}$  was used.

$f(E)^{\text{DFT}}$ , which is not of great consequence when calculating the rates (as the rate is averaged over the distribution).

For iron, which has  $d$  orbitals in the electronic structure, the difference between the various approaches to  $f(E)$  is more evident (shown in Fig. 8). At  $T_e = 1$  eV [Fig. 8(a)], we observe the expected difference between the  $f(E)^{\text{MB}}$  and the  $f(E)^{\text{FEG}}$ , albeit with an electron density higher than that of aluminum and hence a higher Fermi level. For  $f(E)^{\text{DFT}}$ , however, the presence of localized  $d$  orbitals makes peaks in the DOS at lower energies, highlighting a sharp contrast between the  $f(E)^{\text{DFT}}$  and the  $f(E)^{\text{FEG}}$  approaches. At higher temperatures [ $T_e = 20$  eV in Fig. 8(b)], we observe the convergence of the  $f(E)^{\text{MB}}$  and  $f(E)^{\text{FEG}}$  to similar shapes as expected, however, the  $f(E)^{\text{DFT}}$  for iron at this temperature still shows large differences due to the  $d$ -orbital peaks that accumulate electrons at lower energies.

We examine how the  $f(E)$  affects the correction factors in Sec. IV.

#### IV. CORRECTION FACTORS FOR IRON AND ALUMINUM

In this section we present calculations of the correction factor, CF, for iron and aluminum and compare them to the predictions of those when an FEG is assumed. To calculate the degenerate rates for iron and aluminum, we use the element specific DOS presented in Sec. III, the Fermi-Dirac probabil-

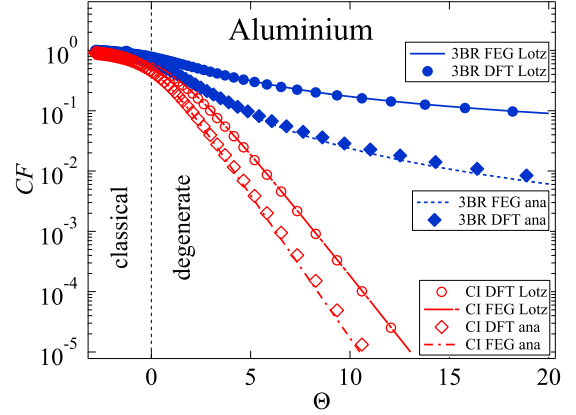


FIG. 9. Correction factors, CF, versus degeneracy,  $\Theta$ , for an aluminum DOS calculated by DFT (symbols) and an FEG (lines). Values of CF are shown for three-body recombination (filled symbols) and collisional ionization (open symbols) for the analytical and Lotz cross sections.

ity distribution function to define  $f(E)$ , and the corresponding blocking factors using Eq. (8).

First, we compare the calculations of the CF for an aluminum DOS and the FEG approximation in Fig. 9. The degenerate and classical regimes can be separated by negative and positive values of  $\Theta$ , respectively. In Fig. 9 the CF values are shown, calculated using the FEG approximation (shown as lines) and the aluminum  $f(E)$  (shown as symbols). The overall trend is a decrease in the collisional ionization and recombination rate as a function of the increasing degeneracy. Larger corrections are evident for collisional ionization, which is attributed to Pauli blocking of the two outgoing electrons emitted during collisional ionization. As the temperature decreases, the ionizing electrons are just above the ionization energy, resulting in ejected electrons that are more prone to Pauli blocking. On the contrary, the effect of Pauli blocking on the three-body recombination rate is minimal for the ionization energies in this study. For example, solid aluminum has an ionization energy of 72 eV, and during three-body recombination the ejected electron will have an energy of at least 72 eV and states at this energy will not be occupied or subject to Pauli blocking. Figure 9 suggests that the CF values calculated using  $f(E)^{\text{DFT}}$  and  $f(E)^{\text{FEG}}$  are very similar. Only small differences, which are orders of magnitude smaller than the total correction factor, occur for the analytical cross-section values. Comparing the electron distributions of the FEG and aluminum, despite small differences at around 40 eV, they are very similar and the impact on the CF values are minimal. This shows that the FEG approximation is valid for calculating degeneracy correction factors of elements with simple free-electron structures, such as aluminum.

In Fig. 10, we compare the CF values calculated with the FEG approximation to those calculated using the iron DOS. In the degenerate regime ( $\Theta > 5$ ), the values of CF calculated using the FEG and the iron DOS from DFT are somewhat comparable, yet differences are evident. The CF values of three-body recombination are about three times lower than the FEG approximation for both cross sections. For collisional ionization, the iron CF values are about 5 times lower than



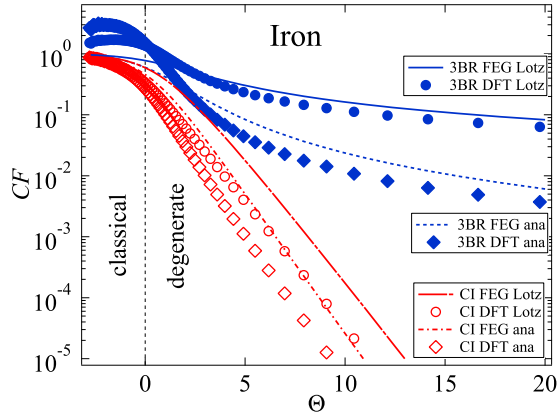


FIG. 10. Correction factors,  $CF$ , versus degeneracy,  $\Theta$ , for an iron DOS calculated by DFT (symbols) and an FEG (lines).  $CF$  values are shown for three-body recombination (filled symbols) and collisional ionization (open symbols) for two different cross sections.

the FEG approximations. To understand this, we recall that for the same  $n_e$  and  $T_e$ , the chemical potential,  $\mu$ , is uniquely defined by the DOS and is element dependent (see Figs. 2 and 3). Therefore, two different elements with the same  $\Theta$  will have different temperatures. For example a solid iron plasma with a degeneracy of  $\Theta = 8.4$  has a temperature of  $T_e = 1$  eV, whereas an FEG plasma with the same electron density and a degeneracy of  $\Theta = 8.4$  has a temperature of  $T_e \approx 3.3$  eV. The lower  $CF$  values in the region where  $\Theta > 5$  for iron are therefore due to the lower temperatures for the same  $\Theta$  compared to the FEG. The lower temperatures correspond to lower degenerate collisional rates for iron and, therefore, smaller  $CF$  values relative to the FEG.

In the lower and intermediate degeneracy regime, from  $\Theta = -3$  to  $\Theta = 2$ , we note a deviation from the general FEG trend in Fig. 10. In this region, from  $\Theta = -3$  to  $\Theta = 2$ , the three-body recombination correction factors are higher than those predicted by the FEG approximation for both the Lotz and the analytical cross sections. Convergence to the classical rate ( $CF \approx 1$ ) occurs at high temperatures with the FEG, but divergence from this trend is evident for three-body recombination in Fig. 10 for iron and has not been previously reported. To gain insight into this behavior we examine the  $f(E)$  for iron in the degenerate regime [Fig. 8(a)] and the classical regime [Fig. 8(b)]. In the degenerate regime [Fig. 8(a)],  $f(E)^{MB}$  allows many more electrons at lower energies than the  $f(E)^{FEG}$  or  $f(E)^{DFT}$  distributions; hence the reduction of three-body recombination in the degenerate regime. In the classical regime shown in Fig. 8(b) the large number of states available in the  $d$  orbitals in the  $f(E)^{DFT}$  results in an accumulation of electrons at lower energies. This accumulation does not occur in  $f(E)^{FEG}$ . The favoring of lower electron energies in the three-body recombination process (see Fig. 5) increases the rate of three-body recombination to above the classical one, leading to values of  $CF \geq 1$ . The persisting differences between the classical and the degenerate electron energy distributions in iron even at higher temperatures explain the absence of conversion to unity of the  $CF$  for three-body recombination in the classical regime. For collisional ionization, however, the cross-section sensitivity to

the electron energy is less pronounced (see Fig. 4) and the convergence of the classical and degenerate rates is observed at higher temperatures,  $CF \approx 1$ .

## V. CONCLUSIONS

Free-electron degeneracy is prevalent in a multitude of terrestrial and astrophysical plasmas. It shapes the electron energy distribution and can block energy transitions due to quantum effects. These effects can inhibit collisional processes such as impact ionization and three-body recombination. We have followed the approach of previous studies [4,18,19] and calculated correction factors to classical collisional rates in order to account for degeneracy in a tractable manner. We find a reduction in the collisional rates with increasing degeneracy, which is far more drastic for collisional ionization due to Pauli blocking of the outgoing electrons. Three-body recombination, however, is not sensitive to Pauli blocking for ionization energies greater than a few times the Fermi level. Unlike other studies that assume an FEG, we have used more realistic electronic structures from DFT to calculate the correction factors. Comparing the correction factors of the FEG and aluminum, only minor differences are noted. This is unsurprising, as the FEG is representative of typical  $s$ - $p$  metals, such as aluminum. This is evident in Fig. 7, where we compare the electron distributions of DFT, MB, and FEG at two temperatures. Therefore, for similar electronic structures the FEG is an appropriate approximation for the degeneracy correction factors of the collisional rates. However, for elements that exhibit a strong deviation from the FEG approximation, such as iron, the corrections can deviate significantly from those calculated using the FEG. These differences occur for two reasons: first, the differences in  $\mu$  for iron and the FEG under the same conditions, causing an overall shift in the degeneracy parameter,  $\Theta$ ; and second, the difference in electron distributions,  $f(E)$ , between iron and the FEG results at different collisional rates for both distributions.

In particular, in the transition between the classical and the degenerate regimes,  $\Theta \approx -2.5$  to 1, the three-body recombination is above that predicted classically due to the accumulation of electrons at lower energies for iron, favoring three-body recombination. This demonstrates the persistence of quantum effects even in regimes considered to be nondegenerate, highlighting the need for careful consideration of quantum corrections even under conditions normally considered classical. The implication of this is, for example, that an iron plasma at solid density and  $T_e = 20$  eV would have a three-body recombination rate about three times higher than, and a collisional ionization rate about one-half, the rate predicted by classical theory, resulting in a plasma that is far less collisionally ionized than predicted classically. Experimental data exist for degeneracy effects in aluminum [20], whereas experimental evidence of this effect for more complex elements such as iron is absent. In the degenerate regime, the standard correction factors calculated using the FEG model already present a significant improvement in accuracy compared to classical predications. The role of the plasma density in shaping the collisional cross sections can be accounted for in certain respects, for example, lowering the

ionization energy through ionization potential depression. However, changes in the shape of the cross section in high-energy-density plasmas are more difficult to account for. Including degeneracy effects in the free-electron distribution constitutes a significant improvement in the calculation of the collisional rates, yet subtle density effects in the cross-section shapes are not accounted for. Using the DOS from DFT for the free-electron distribution over a wider range of temperatures and densities requires an individual calculation for each set of conditions, including bound states. Encouragingly, in modern DFT codes a DOS calculation that captures the important features of the DOS is not computationally prohibitive. Further experiments will determine the accuracy of predictions for other elements and guide CR codes to be more accurate in a wider range of plasma conditions.

## ACKNOWLEDGMENTS

We acknowledge support from Fundação para a Ciência e a Tecnologia (FCT) projects 02/SAICT/2017/31868, COST Action CA17126, and Laserlab-Europe EU-H2020 654148. This work was supported by the European Union's Horizon 2020 research and innovation program (VOXEL H2020-FETOPEN-2014-2015-RIA 665207). This work was carried out within the framework of EUROfusion Enabling Research Project ENR-IFE19.CEA-01, "Study of Direct Drive and Shock Ignition for IFE: Theory, Simulations, Experiments, Diagnostics Development," and received funding from the Euratom research and training program. The views and opinions expressed herein do not necessarily reflect those of the European Commission.

- 
- [1] W. Pauli, Über den einfluß der geschwindigkeitsabhängigkeit der elektronenmasse auf den zeemaneffekt, *Z. Phys.* **31**, 373 (1925).
- [2] A. Hayes, M. Gooden, E. Henry, G. Jungman, J. Wilhelmy, R. Rundberg, C. Yeamans, G. Kyrala, C. Cerjan, D. Danielson *et al.*, Plasma stopping-power measurements reveal transition from non-degenerate to degenerate plasmas, *Nat. Phys.* **16**, 432 (2020).
- [3] M. N. Saha, On a physical theory of stellar spectra, *Proc. R. Soc. London Ser. A* **99**, 135 (1921).
- [4] Y. Ralchenko, *Modern Methods in Collisional-Radiative Modeling of Plasmas* (Springer, Berlin, 2016), Vol. 90.
- [5] H.-K. Chung, M. H. Chen, W. L. Morgan, Y. Ralchenko, and R. W. Lee, Flychk: Generalized population kinetics and spectral model for rapid spectroscopic analysis for all elements, *High Energy Density Phys.* **1**, 3 (2005).
- [6] M. F. Gu, The flexible atomic code, *Can. J. Phys.* **86**, 675 (2008).
- [7] A. Bar-Shalom, M. Klapisch, and J. Oreg, Hullac, an integrated computer package for atomic processes in plasmas, *J. Quant. Spectrosc. Radiat. Transfer* **71**, 169 (2001).
- [8] S. B. Hansen, E. C. Harding, P. F. Knapp, M. R. Gomez, T. Nagayama, and J. E. Bailey, Fluorescence and absorption spectroscopy for warm dense matter studies and ICF plasma diagnostics, *Phys. Plasmas* **25**, 056301 (2018).
- [9] C. A. Iglesias and R. W. Lee, Density effects on collisional rates and population kinetics, *J. Quant. Spectrosc. Radiat. Transfer* **58**, 637 (1997).
- [10] D. O. Gericke, M. Schlanges, and T. Bornath, Stopping power of nonideal, partially ionized plasmas, *Phys. Rev. E* **65**, 036406 (2002).
- [11] M. Schlanges and T. Bornath, Ionization and recombination coefficients for a dense nonideal hydrogen plasma: Effects of screening and degeneracy, *Physica A* **192**, 262 (1993).
- [12] Z. Q. Wu, G. X. Han, J. Yan, and J. Q. Pang, Plasma effects on electron impact ionization, *J. Phys. B: At. Mol. Opt. Phys.* **35**, 2305 (2002).
- [13] A. V. Lankin and G. E. Norman, Collisional recombination in strongly coupled plasmas, *J. Phys. A: Math. Theor.* **42**, 214042 (2009).
- [14] Y. Hahn, Plasma density effects on the three-body recombination rate coefficients, *Phys. Lett. A* **231**, 82 (1997).
- [15] O. Ciricosta, S. Vinko, B. Barbrel, D. Rackstraw, T. Preston, T. Burian, J. Chalupský, B. I. Cho, H.-K. Chung, G. Dakovski *et al.*, Measurements of continuum lowering in solid-density plasmas created from elements and compounds, *Nat. Commun.* **7**, 11713 (2016).
- [16] O. Ciricosta, S. M. Vinko, H.-K. Chung, B. I. Cho, C. R. D. Brown, T. Burian, J. Chalupský, K. Engelhorn, R. W. Falcone, C. Graves, V. Hájková, A. Higginbotham, L. Juha, J. Krzywinski, H. J. Lee, M. Messerschmidt, C. D. Murphy, Y. Ping, D. S. Rackstraw, A. Scherz, W. Schlotter, S. Toleikis, J. J. Turner, L. Vysin, T. Wang, B. Wu, U. Zastra, D. Zhu, R. W. Lee, P. Heimann, B. Nagler, and J. S. Wark, Direct Measurements of the Ionization Potential Depression in a Dense Plasma, *Phys. Rev. Lett.* **109**, 065002 (2012).
- [17] S. B. Hansen, H.-K. Chung, C. Fontes, Y. Ralchenko, H. Scott, and E. Stambulchik, Review of the 10th Non-LTE Code Comparison Workshop, *High Energy Density Phys.* **35**, 100693 (2020).
- [18] G. Tallents, Free electron degeneracy effects on collisional excitation, ionization, de-excitation and three-body recombination, *High Energy Density Phys.* **20**, 9 (2016).
- [19] G. Tallents, *An Introduction to the Atomic and Radiation Physics of Plasmas* (Cambridge University Press, Cambridge, UK, 2018).
- [20] G. O. Williams, H.-K. Chung, S. Künzel, V. Hilbert, U. Zastra, H. Scott, S. Daboussi, B. Iwan, A. I. Gonzalez, W. Boutu, H. J. Lee, B. Nagler, E. Granados, E. Galtier, P. Heimann, B. Barbrel, R. W. Lee, B. I. Cho, P. Renaudin, H. Merdji, P. Zeitoun, and M. Fajardo, Impact of free electron degeneracy on collisional rates in plasmas, *Phys. Rev. Res.* **1**, 033216 (2019).
- [21] P. A. M. Dirac, On the theory of quantum mechanics, *Proc. R. Soc. London Ser. A* **112**, 661 (1926).
- [22] E. Fermi, Sulla quantizzazione del gas perfetto monoatomico, *Rend. Lincei* **3**, 145 (1926).
- [23] A. Sommerfeld, Zur Elektronentheorie der Metalle auf Grund der Fermischen Statistik, *Z. Phys.* **47**, 1 (1928).
- [24] V. Aslanyan and G. J. Tallents, Ionization rate coefficients in warm dense plasmas, *Phys. Rev. E* **91**, 063106 (2015).

- [25] A. Levy, P. Audebert, R. Shepherd, J. Dunn, M. Cammarata, O. Ciricosta, F. Deneuville, F. Dorchies, M. Fajardo, C. Fourment *et al.*, The creation of large-volume, gradient-free warm dense matter with an x-ray free-electron laser, *Phys. Plasmas* (1994–present) **22**, 030703 (2015).
- [26] S. Vinko, O. Ciricosta, B. Cho, K. Engelhorn, H.-K. Chung, C. Brown, T. Burian, J. Chalupský, R. Falcone, C. Graves *et al.*, Creation and diagnosis of a solid-density plasma with an x-ray free-electron laser, *Nature* **482**, 59 (2012).
- [27] G. O. Williams, S. Künzel, S. Daboussi, B. Iwan, A. I. Gonzalez, W. Boutu, V. Hilbert, U. Zastrau, H. J. Lee, B. Nagler, E. Granados, E. Galtier, P. Heimann, B. Barbrel, G. Dovillaire, R. W. Lee, J. Dunn, V. Recoules, C. Blancard, P. Renaudin, A. G. de la Varga, P. Velarde, P. Audebert, H. Merdji, P. Zeitoun, and M. Fajardo, Tracking the ultrafast XUV optical properties of x-ray free-electron-laser heated matter with high-order harmonics, *Phys. Rev. A* **97**, 023414 (2018).
- [28] D. E. Fratanduono, R. F. Smith, S. J. Ali, D. G. Braun, A. Fernandez-Pañella, S. Zhang, R. G. Kraus, F. Coppari, J. M. McNaney, M. C. Marshall, L. E. Kirch, D. C. Swift, M. Millot, J. K. Wicks, and J. H. Eggert, Probing the Solid Phase of Noble Metal Copper at Terapascal Conditions, *Phys. Rev. Lett.* **124**, 015701 (2020).
- [29] W. Lotz, Electron-impact ionization cross-sections and ionization rate coefficients for atoms and ions from hydrogen to calcium, *Z. Physik* **216**, 241 (1968).
- [30] W. Lotz, An empirical formula for the electron-impact ionization cross-section, *Z. Physik* **206**, 205 (1967).
- [31] M. Belkhiri and M. Poirier, Analysis of density effects in plasmas and their influence on electron-impact cross sections, *Phys. Rev. A* **90**, 062712 (2014).
- [32] J. Oxenius, *Kinetic Theory of Particles and Photons: Theoretical Foundations of Non-LTE Plasma Spectroscopy* (Springer Science & Business Media, New York, 2012), Vol. 20.
- [33] N. D. Mermin, Thermal properties of the inhomogeneous electron gas, *Phys. Rev.* **137**, A1441 (1965).
- [34] K. Burke, J. C. Smith, P. E. Grabowski, and A. Pribram-Jones, Exact conditions on the temperature dependence of density functionals, *Phys. Rev. B* **93**, 195132 (2016).
- [35] V. V. Karasiev, L. Calderín, and S. B. Trickey, Importance of finite-temperature exchange correlation for warm dense matter calculations, *Phys. Rev. E* **93**, 063207 (2016).
- [36] F. Graziani, *Frontiers and Challenges in Warm Dense Matter* (Springer Science & Business, New York, 2014), Vol. 96.
- [37] G. Kresse and J. Furthmüller, Efficient iterative schemes for ab initio total-energy calculations using a plane-wave basis set, *Phys. Rev. B* **54**, 11169 (1996).
- [38] G. Kresse and J. Furthmüller, Efficiency of ab-initio total energy calculations for metals and semiconductors using a plane-wave basis set, *Comput. Mater. Sci.* **6**, 15 (1996).
- [39] G. Kresse and J. Hafner, Ab initio molecular dynamics for liquid metals, *Phys. Rev. B* **47**, 558 (1993).
- [40] G. Kresse and J. Hafner, Ab initio molecular-dynamics simulation of the liquid-metal–amorphous-semiconductor transition in germanium, *Phys. Rev. B* **49**, 14251 (1994).
- [41] G. Kresse and D. Joubert, From ultrasoft pseudopotentials to the projector augmented-wave method, *Phys. Rev. B* **59**, 1758 (1999).
- [42] P. E. Blöchl, Projector augmented-wave method, *Phys. Rev. B* **50**, 17953 (1994).
- [43] J. P. Perdew, K. Burke, and M. Ernzerhof, Generalized Gradient Approximation Made Simple, *Phys. Rev. Lett.* **77**, 3865 (1996).
- [44] D. M. Ceperley and B. J. Alder, Ground State of the Electron Gas by a Stochastic Method, *Phys. Rev. Lett.* **45**, 566 (1980).
- [45] H. J. Monkhorst and J. D. Pack, Special points for Brillouin-zone integrations, *Phys. Rev. B* **13**, 5188 (1976).